Journal of Zhejiang University-SCIENCE A in press
www.jzus.zju.edu.cn; www.springer.com/journal/11582
E-mail: jzus_a@zju.edu.cn

Research Article
https://doi.org/10.1631/jzus.A2500352

Aerodynamic optimization of an externally tilted hex-rotor hovering UAV

Hengxing YANG[1], Yao LEI[1,2]✉, Jifu HU[1], Guobin SHI[3]

[1]*School of Mechanical Engineering and Automation, Fuzhou University, Fuzhou 350116, China*
[2]*Key Laboratory of Fluid Power and Intelligent Electro-Hydraulic Control, Fuzhou University, Fuzhou 350116, China*
[3]*School of Intelligent Systems Engineering, Sun Yat-sen University, Shenzhen 518000, China*

Abstract: We investigate the aerodynamic performance and flow field synergy of an externally tilted hex-rotor unmanned aerial vehicle (UAV) in hovering mode, aiming to enhance its hovering efficiency through tailored flow interactions. Experimental measurements and computational fluid dynamics (CFD) simulations are combined to examine the effects of rotor spacing ratio (i = 0.5–0.83) and tilt angle (θ = 0°–40°) on thrust, power consumption, figure of merit (FM), and power loading (PL), with particular emphasis on the underlying aerodynamic coupling mechanisms. The results demonstrate that the optimal configuration (i = 0.56, θ = 24°) achieves a 5.43% thrust increase, a 2.73% power reduction, an 11.15% improvement in FM, and a 3.77% enhancement in PL compared to a conventional planar configuration. Flow field analyses reveal that moderate tilting (θ = 24°) promotes downwash convergence and strengthens vortex coupling, thereby increasing the effective flow velocity while minimizing inter-rotor turbulent interference. Furthermore, the spacing ratio of i = 0.56 effectively balances the reduction of detrimental flow interference with the promotion of beneficial flow interactions, as evidenced by stabilized primary vortex structures and constrained recirculation zones in the CFD simulations. This work highlights how the aerodynamic optimization of non-planar rotor configurations critically dependent on the synergistic control of tilt-induced flow deflection and spacing-dependent interference, and establishes a theoretical framework for understanding multi-rotor flow dynamics; as such, the findings may aid the design of efficient rotor systems for UAVs.

Key words: UAV; Aerodynamic performance; Hover efficiency; Inter-rotor interference; CFD

1 Introduction

In recent years, aerodynamic design of unmanned aerial vehicles (UAVs) has evolved from conventional co-planar rotor configurations to spatially distributed configurations. This shift is being driven by growing demands for enhanced payload capacity and mission-adaptable maneuverability, where rotor flow interactions are now recognized as a critical factor governing overall performance. UAVs are consequently finding widespread application in forestry, agriculture, commerce, and defense, and other fields (Mu et al., 2023; Prabhu et al., 2024; Su et al., 2023; Marris, 2013; Frachetti et al., 2024; Jiang et al., 2023; Wang et al., 2024). Parallel advancements in manufacturing, such as combining additive manufacturing with generative design, further support this trend by enabling lightweight and efficient structures (Maisto et al., 2025). However, conventional planar rotor configurations are inherently constrained by size limitations and suboptimal aerodynamic efficiency, which primarily arises from unregulated inter-rotor flow interference. This hinders operational effectiveness in complex environments, thus highlighting the need for innovative rotor configurations that can leverage controlled flow dynamics.

Prior research on hex-rotors has predominantly focused on control strategies. For instance, Yao et al. (2018) developed sliding mode controllers for

✉Yao LEI, yaolei@fzu.edu.cn
Hengxing YANG, https://orcid.org/0009-0006-0150-6398
Yao LEI, https://orcid.org/0000-0002-4764-2081
Jifu HU, https://orcid.org/0009-0009-1773-2121
Guobin SHI, https://orcid.org/0009-0001-6512-0172

Received July 26, 2025; Revision accepted Jan. 6, 2026;
Crosschecked

tilted-rotor systems, emphasizing disturbance rejection; Yang et al. (2017) proposed adaptive backstepping frameworks for trajectory tracking; Sina et al. (2021) integrated optimization with sliding mode control for path planning; and Ibuki et al. (2022) leveraged Gaussian processes to compensate for modeling uncertainties. While these studies improved operational robustness, they largely treated aerodynamic forces as predetermined inputs, thereby overlooking the underlying flow mechanisms that govern thrust and power.

Concurrently, efforts to characterize multirotor aerodynamics have yielded insights into specific configurations. In one study, Li et al. (2019) experimentally investigated the aerodynamic interference mechanisms in non-planar rotor pairs for a hexacopter, quantifying the coupled effects of tilt angle ($10°-50°$), rotor spacing ($1.0D-1.8D$), and wind speed (0 – 4 m/s); they identified optimal parameters that reduced parasitic power losses by 18.7%. Bohorquez et al. (2003) conducted an experimental aerodynamic analysis on four different rotor types for compact multi-rotor aircraft. Moreover, numerical simulations were performed to investigate rotor–rotor aerodynamic disturbances by Piccinini et al. (2020). Also, Luo et al. (2015) presented a mathematical model for forward flight considering the interference of the rotor in hovering. Wang et al. (2019) experimentally demonstrated the influence of mounting configurations on a single rotor's aerodynamic and acoustic characteristics. Lei et al. (2018; 2021) studied the impact of rotor spacing on the aerodynamic characteristics of multi-rotor UAVs using both experimental testing and computational fluid dynamics (CFD). Chen et al. (2019) focused on aerodynamic measurements of a non-planar configuration in hovering.

Notably, existing work on non-planar rotors lacks detailed, validation analysis of how tilt-induced flow deflection and spacing-dependent interference synergistically modulate vortex dynamics, downwash coherence, and overall hovering efficiency. This gap hinders the rational design of next-generation multirotor systems. To address this, we employ an integrated experimental and CFD simulation approach to dissect the synergistic effects in an externally tilted hex-rotor. Beyond identifying optimal parameters, we provide detailed flow field analyses to uncover the underlying mechanisms of downwash convergence and vortex coupling, thus distinguishing our work from previous parametric studies.

In particular, we aim to enhance the payload capacity and aerodynamic efficiency of externally tilted hex-rotor systems by fundamentally unraveling how flow interactions, as governed by rotor spacing and tilt angle, dictate hovering performance. We perform optimization across a broad parameter space, with the core objective of balancing the reduction of detrimental turbulent interference against the promotion of beneficial flow coupling. Through visualization and analysis of downwash patterns, vortex dynamics, and pressure distributions, we establish a cause-and-effect fluid-mechanical framework. This framework helps identify optimal design configurations, and provides actionable insights for bridging aerodynamic design with control strategy.

A conventional hex-rotor configuration aligns all rotors in a single horizontal plane, where flow interactions are dominated by unstructured downwash mixing and vortex interference. In contrast, an externally tilted configuration inclines rotors outward by an angle of θ, creating a spatially distributed architecture that actively reshapes the flow field. This fundamental difference highlights the tilted design's potential to exploit controlled aerodynamic synergy, particularly through downwash convergence and vortex coupling; these are the central investigative themes of this work.

Our investigation focuses on a prototype system with a rotor diameter D = 240 mm and a rotational speed Ω = 5,500 r/min. While the fundamental fluid-mechanical principles revealed are general, the optimal configuration is system-specific.

Overall, this study makes three key contributions:

1. It reveals the fundamental fluid-dynamic mechanisms underlying the improved hovering efficiency of externally tilted hex-rotor designs relative to conventional planar designs. We demonstrate how downwash convergence, enhanced vortex coupling, and mitigated turbulent dissipation collectively augment aerodynamic performance through detailed flow field analyses.
2. It elucidates the synergistic interplay between

the rotor spacing ratio i and tilt angle θ in governing thrust generation. We identify how this synergy balances the reduction of detrimental inter-rotor flow interference against the promotion of beneficial aerodynamic interactions, with a specific focus on pressure gradient distributions and primary vortex structural stability.

3. It identifies the optimal combination of rotor spacing ratio (i = 0.56) and tilt angle (θ = 24°) that maximizes hovering efficiency. This optimization is validated through integrated experimental measurements and CFD simulations; it leads to stabilized vortex dynamics, constrained recirculation zones, and enhanced downwash coherence.

The structure of this paper is as follows. Section 2 details the geometric model and theoretical foundations. Section 3 describes the experimental and computational methodologies. In Section 4 we present and discusses the results, linking performance metrics to flow field mechanisms. Finally, Section 5 offers conclusions and outlines future work.

2 Modeling and theory

2.1 Model design

The structure of the externally tilted hex-rotor UAV analyzed in this study is illustrated in Fig. 1. The adjacent arms are spaced at 60° intervals with equal arm lengths, and each rotor is tilted at an angle of θ. The adjacent rotor spacing is denoted as L, and the rotor diameter is D (mm). The system is comprised of six rotors arranged in an alternating configuration of P-N-P-N-P-N, where "P" denotes clockwise rotation (positive) and "N" counterclockwise rotation (negative); Ω is the rotor speed (r/min).

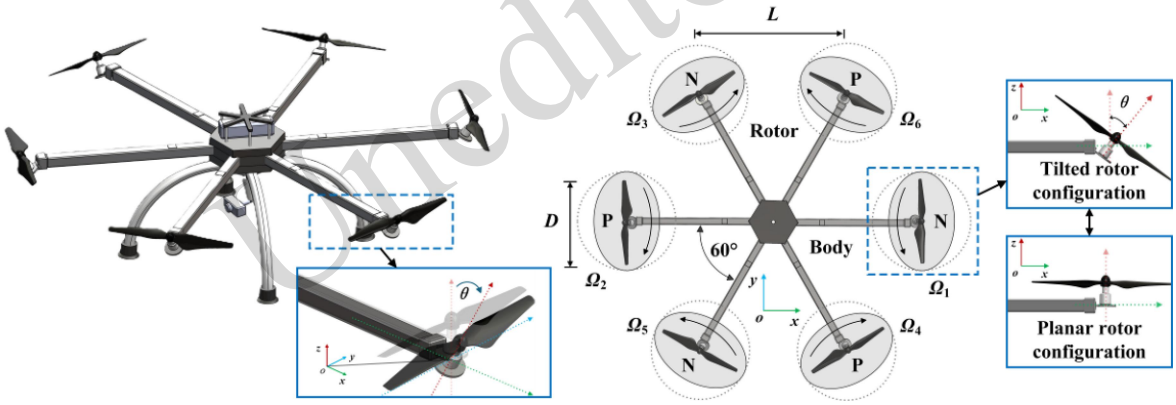

Fig. 1 Structure of the externally tilted hex-rotor UAV

We utilize the DJI 9450 (D = 240 mm) rotor, a size commonly adopted in multi-rotor UAV research (Luan and Lei, 2025). To improve aerodynamic performance, the conventional plastic rotor was replaced with a carbon fiber version, which offers greater stiffness and a higher thrust coefficient (Deters et al., 2017; Garofano-Soldado et al., 2023). Its geometric characteristics are detailed in Fig. S1 of the Electronic Supplementary Material (ESM).

The rotor operation is characterized by a low Reynolds number, given that the free stream speed is neglected (Garofano-Soldado et al., 2022; Jaroslawski et al., 2022). The relevant formulas are presented in Eq. (S1) of the ESM.

2.2 Aerodynamic analysis

Fig. 2 illustrates the details of the externally tilted hex-rotor configuration, revealing the complex coupling between the rotor geometry and the airflow trajectory. The left panel depicts the thrust arrangement, where T_i represents the thrust generated by the i^{th} rotor. The right panel employs streamline visualization to clarify the paths of the incoming flow (upstream of the rotors) and the outgoing wake (downstream), highlighting how tilt-induced deflection reorganizes the velocity field.

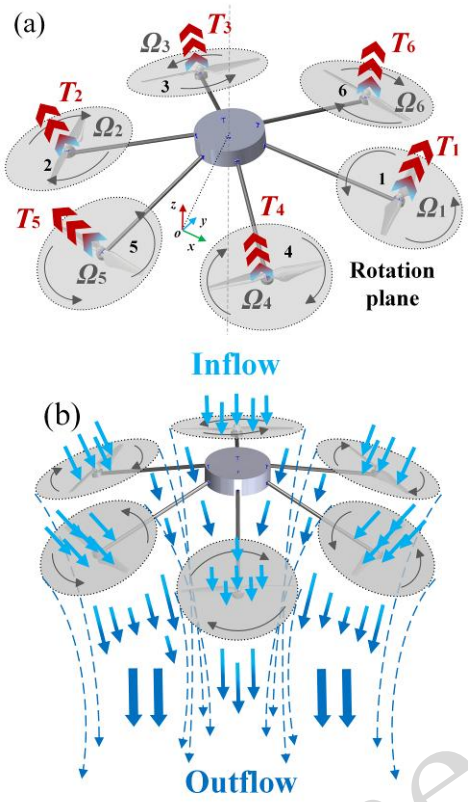

Fig. 2 Thrust and flow field characteristics of UAV

Notably, the externally tilted configuration organizes downwash interactions by aligning the outflow from individual rotors toward a common central region. This design promotes convergent downwash, which establishes a concentrated flow zone beneath the rotor system. The resulting flow convergence increases the axial velocity, enhancing thrust, while simultaneously mitigating cross-stream turbulent mixing. During hovering, the resulting flow field produces a more uniform lift distribution across the rotors, which suppresses oscillations and improves stability. Collectively, these flow mechanisms demonstrate how geometric tilting converts inter-rotor interference into beneficial synergy, which is a central theme in our analysis.

An increase in rotor spacing reduces the overlap between downwash streams and adjacent rotors, thereby weakening the aerodynamic interference that arises from vortex interactions and turbulent mixing; however, excessive spacing compromises system compactness. This represents a critical design trade-off that balances the benefit of reduced flow interference against the penalties of increased size, both of which affect maneuverability and structural efficiency.

For explanation on how the rotor spacing and deflection angle were selected, please refer to Section S1 of the ESM. Also note that a detailed description of the system is provided in Section S2.

3 Methods

3.1 Experimental approach

3.1.1 Experimental setup

To evaluate the variation in the UAV's aerodynamic performance under hovering conditions, an experimental test bench was constructed, inspired by multi-rotor test benches used by NASA (Russell and Conley, 2020). As shown in Fig. 3, the bench measures 1.5 m in length, 1.5 m in width, and 2.0 m in height. Its design enables independent adjustment of the rotor pitch and tilt angles. The rotor was positioned 2 m above the floor to minimize ground effects. Furthermore, during formal testing, the setup was placed over 3 m from the laboratory walls to mitigate potential interference.

The rotor is powered by a brushless DC motor (MSYS LRK 195.03, Yuanhang Technology). The current and voltage are monitored via the DC power supply (RS Pro IPS 3202, Dexin Technology). A Hall-effect sensor enables precise measurement of the RPM for speed control performance evaluation. For the hovering condition, a flexible rotor design was adopted due to the significant influence of rotor flexibility on overall aerodynamic performance. Key sensor specifications are listed in Table S1 in the ESM.

The force transducers and torque sensors used in the experimental setup possess finite physical dimensions, which can disturb the rotor wake. Specifically, their structures may disrupt the downstream flow field of the rotors, leading to local flow separation and a slight distortion of the downwash pattern. To evaluate this effect, CFD simulations were performed explicitly including the geometry of the sensors. These simulations confirm that the primary vortex structures and axial velocity profiles, which are key to thrust generation, remain largely unaffected. Only marginal flow perturbations are observed in the near wake region, within 1*D*

downstream of the rotors. While the sensor size introduces minor flow disturbances, they do not significantly affect overall aerodynamic trends or invalidate the performance improvements observed in the study.

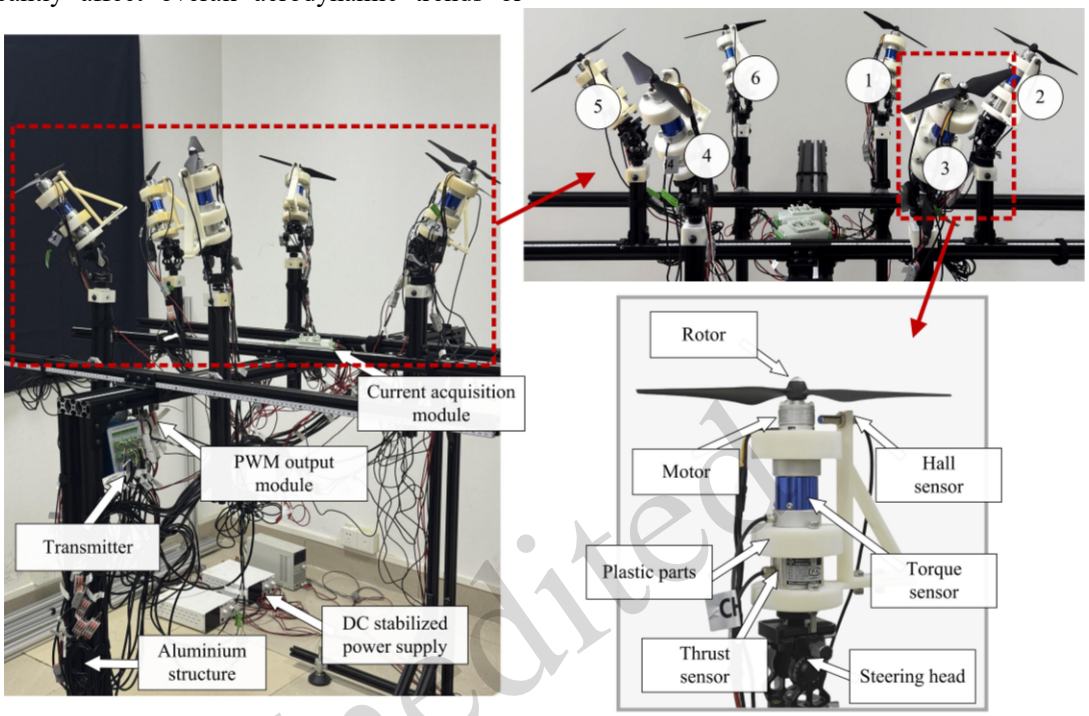

Fig. 3 Experimental setup

Table 1 Parameter values in the experiment

Parameters	Value
Rotor diameter D (mm)	240
Number of blades	2
Weight (kg)	0.025
Material of blades	Carbon fiber
Rotor speed Ω (r/min)	5,500
Rotor spacing ratio i	0.5, 0.56, 0.63, 0.71, 0.83
Tilt angle θ (deg)	0, 8, 16, 24, 32, 40

For each rotor speed, data were collected at a sampling rate of 1,000 Hz over a four-minute duration, with mean values computed to mitigate unsteady effects. The experiments were conducted in a climate-controlled indoor facility under conditions of 25 °C temperature, 53% relative humidity, and 101.3 kPa atmospheric pressure. Each test condition was replicated three times to ensure repeatability and reproducibility of the results. Key experimental parameters are summarized in Table 1.

3.1.2 Variables and performance parameters

All measured variables and their corresponding units are listed in Table S2 of the ESM.

The rotor spacing ratio i is defined as:

$$i = \frac{D}{L}. \tag{1}$$

The rotor diameter D is 240 mm, and L is set within the range of 1.2D to 2.0D. Therefore, the rotor spacing ratio i is set to 0.5, 0.56, 0.63, 0.71, and 0.83.

The thrust and the induced velocity of the rotor are determined using the momentum theorem (Moses et al., 2016):

$$T = 2\pi R^2 \rho v_1^2. \tag{2}$$

$$v_1 = \sqrt{\frac{T}{2\pi R^2 \rho}}. \tag{3}$$

where T is thrust (N), R is rotor radius (mm), ρ is air density (kg/m^3), v_1 is the induced velocity (m/s).

The power consumption associated with the induced velocity is (Quintana et al., 2018):

$$P = Tv_1 \tag{4}$$

Additionally, the power consumption is calculated from the torque as:

$$P = Q\omega = 2\pi nQ. \tag{5}$$

where n is rotational speed (r/s), ω is angular velocity (rad/s), and Q is torque (N·m).

The dimensionless thrust coefficient C_T and power coefficient C_P are defined as follows:

$$C_T = \frac{4T}{\rho A \Omega^2 D^2}, C_P = \frac{8P}{\rho A \Omega^3 D^3}. \tag{6}$$

where A is the rotor disk area (m^2), P is the power consumption (W), and Ω is the rotor's rotational speed (r/min).

The figure of merit (FM) is adopted to quantify the overall efficiency of the UAV system. To further evaluate the payload capacity under power constraints, the concept of power loading (PL) is introduced. Both metrics are influenced by thrust generation and power consumption (Lei et al., 2018). FM and PL are defined as follows:

$$\mathrm{FM} = \frac{C_T^{\frac{3}{2}}}{\sqrt{2}C_P}, \mathrm{PL} = \frac{C_T}{\Omega C_P}. \tag{7}$$

Combining Eq. (9) with Eq. (10) yields an alternative form of the PL:

$$\mathrm{PL} = \frac{T}{P}. \tag{8}$$

According to Eq. (7), it is evident that higher hovering efficiency and enhanced payload capacity can be achieved through an increased FM and a higher PL, which necessitates either greater thrust generation or reduced power consumption. Consequently, thrust T and power consumption P are the key parameters to measure in our experiments. Identical conditions were employed for all configurations in both the experiments and simulations. Note that error and uncertainty analysis is provided in Section S3 of the ESM.

3.2 Simulation approach

3.2.1 Simulation setup

Numerical simulations were performed using the commercial CFD software ANSYS Fluent (version 2021 R1). To simplify the computational model, non-aerodynamic components such as the motor and support arms were omitted. As illustrated in Fig. 4, the complete computational domain consists of three distinct regions: a rotating domain, a stationary domain, and a body of influence (BOI) domain. The BOI was utilized to achieve local mesh refinement, thereby enhancing the simulation accuracy. To minimize ground interference, the UAV was positioned in the upper section of the domain. The stationary domain was defined as a cylinder with a height of 3,600 mm and a diameter of 2,400 mm. Its top surface was set as a velocity inlet, the other external surfaces were set as pressure outlets, and the blade surfaces were defined as no-slip walls.

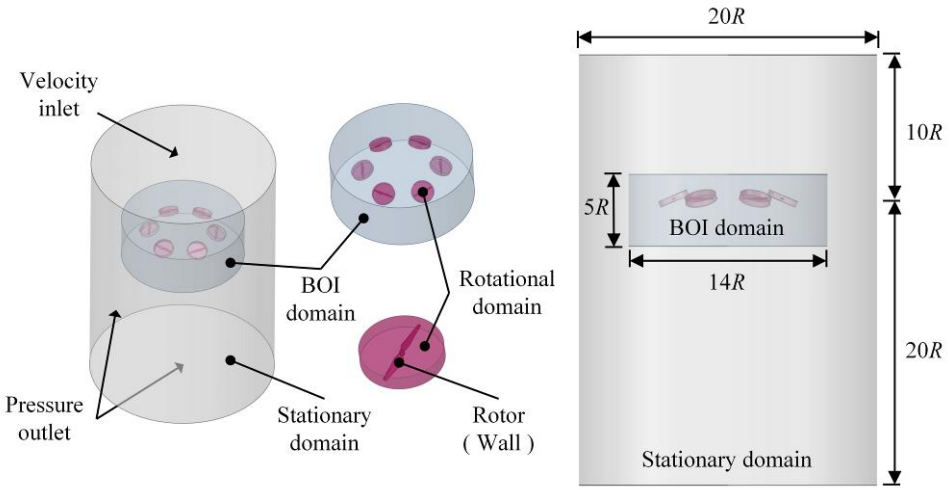

Fig. 4 Computational domain and boundary conditions

Given the presence of incompressible flow, a pressure-based solver was employed. The realizable k–ε model, while robust for broad external flow applications, has a recognized deficiency in resolving flows dominated by strong streamline curvature and rotation. Therefore, the shear stress transport (SST) k-ω model was selected. Its established strengths in predicting adverse pressure gradient flows and separation, which are highly relevant to rotating machinery, make it particularly appropriate for this study (Menter et al., 2003). The model's validity is also supported by its successful application and strong correlation with experimental measurements in related work (Farajollahi and Rostami, 2021; Cerny and Breitsamter, 2020).

The simulations consisted of two phases: a steady-state initialization for 1,200 iterations followed by a transient analysis for 1300 iterations, totaling 2,500 physical time steps. The physical time step size was set to $\Delta t = 9.09\times10^{-5}$ s. At the operational speed of 5,500 r/min (575.96 rad/s), this corresponds to an angular advancement of approximately 3.0° per time step, ensuring the Courant-Friedrichs-Lewy (CFL) condition for numerical stability was satisfied. The sliding mesh interface was updated after every 60° of rotation to balance accuracy and computational efficiency. The total simulated physical time was approximately 0.227 seconds (equivalent to over 20 complete rotor revolutions), ensuring the flow field reached a statistically stationary state. This approach aligns with the methodology of Sheidani et al. (2023), who emphasized the necessity of simulating enough rotational cycles to achieve statistical convergence in rotating machinery simulations.

3.2.1 Mesh generation and independence study

A hybrid computational approach was employed to simulate the rotor's rotation. The multiple reference frame (MRF) model was first used to obtain an efficient steady state solution for the flow field. This solution then served as the initial condition for a high-fidelity transient analysis using the sliding mesh method (SMM), which accurately captures unsteady rotor-rotor aerodynamic interactions and wake development (Luo et al., 2023). The volume meshes for the stationary and rotating domains were generated separately within ANSYS Fluent using the Poly-Hexcore scheme. This method combines hexahedral elements in the core region with polyhedral elements elsewhere, enhancing solution accuracy and numerical stability while maintaining computational efficiency.

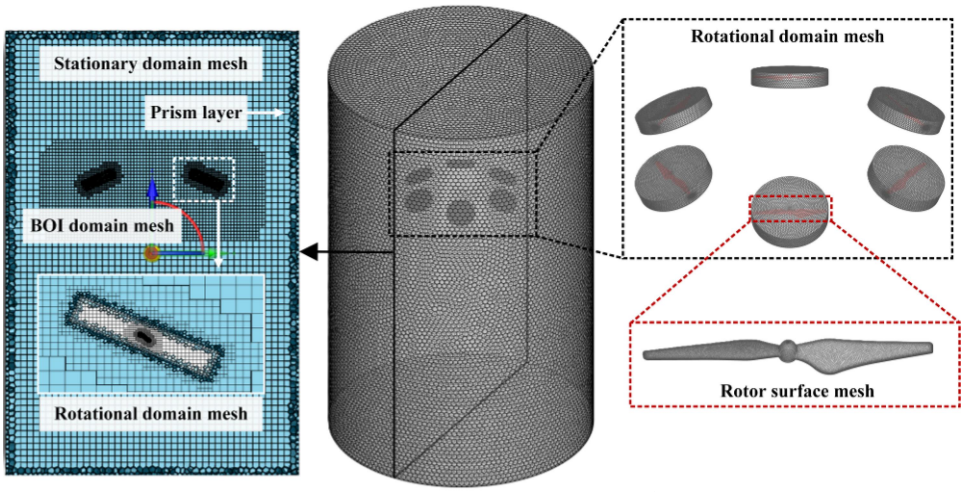

Fig. 5 Mesh distribution

Specifically, the computational domain was partitioned into three distinct subdomains: (1) the rotational domain, in which each rotor was enclosed within an independent cylindrical sub-domain (diameter 260 mm, height 100 mm) rotating at 5,500 r/min to accurately resolve the flow field around the individual rotors; (2) BOI domain, configured as a cylindrical region encompassing all rotors (diameter 2,240 mm, height 600 mm) and discretized using isotropic refinement with a nominal cell size of 4 mm to adequately capture vortex interactions among the rotors; and (3) the stationary domain, representing the outer cylindrical region, which was meshed with structured hexahedral elements and a gradual expansion ratio of 1.1 to ensure a smooth transition and minimize numerical dissipation. To satisfy the near-wall resolution requirements of the SST k-ω turbulence model, for which the target y^+ value was maintained below unity high-quality prism layers were generated on the surrounding frame. The mesh generation process adhered to the best practices for complex flow simulations, as established in the recent work of Gerdroodbary et al. (2024).

Verification of the mesh independence is detailed in Section S4 of the ESM.

Based on our mesh independence study, Mesh 4 was ultimately selected for all subsequent simulations. Fig. 5 displays the final computational mesh, which incorporates local refinement near the rotor surface, the blade edges, and the wake interface. The orthogonal quality for all meshes exceeds 0.25, confirming acceptable mesh quality and reliability for the numerical simulations.

4 Results and discussion

This section outlines the experimental and simulation results. Note that detailed validation analysis is provided in Section S5 of the ESM.

4.1 Experimental results

As illustrated in Fig. 6, the measured thrust and power consumption demonstrate clear dependencies on the rotor spacing ratio i and tilt angle θ. Thrust varies non-monotonically with decreasing i, showing modest improvements at intermediate tilt angles (16° and 24°) within certain spacing ranges. In contrast, power consumption generally decreases with decreasing i. Notably, the configuration with $i = 0.56$ and $\theta = 24°$ achieves the highest thrust of 22.31 N and the lowest power of 202.75 W. This performance optimum results from a balanced interaction of flow mechanisms: spacing at this ratio mitigates cross-stream turbulent interference, while the 24° tilt promotes beneficial downwash convergence and vortex coupling. The synergy between reduced lateral disturbance and enhanced flow coordination leads to increased thrust and reduced power consumption, highlighting the pivotal role of geometric parameters in modulating aerodynamic efficiency.

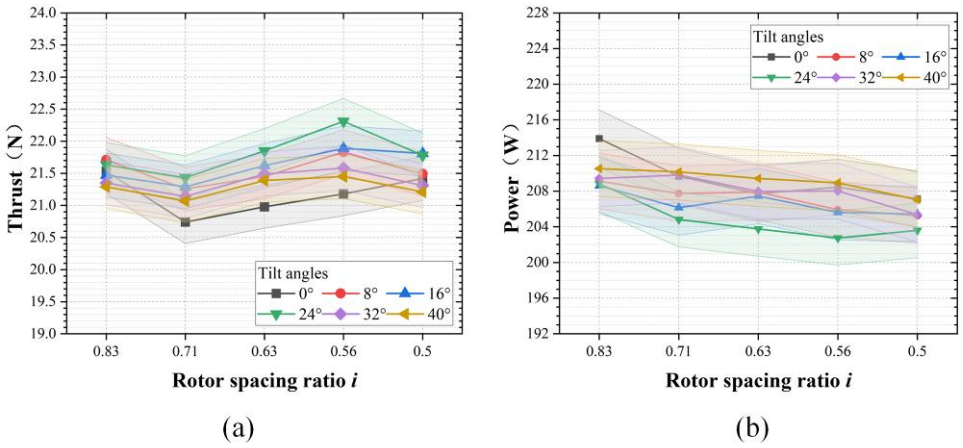

(a) (b)

Fig. 6 Thrust and power with different rotor spacing ratios and tilt angles (error bars represent 95% confidence intervals based on triplicate measurements): (a) thrust variation; (b) power variation

Fig. 7 compares the thrust and power characteristics of the externally tilted hex-rotor with the conventional planar configuration, revealing key performance distinctions that are fundamentally rooted in different in flow field patterns. Specifically, when operating at optimized spacing ratios, the tilted design produces higher thrust than the planar design, an advantage attributed to its ability to harness constructive flow interactions. At the smallest spacing (i = 0.83), configurations with large tilts (θ = 40° and 32°) exhibit thrust reductions of 1.11% and 0.84%, respectively. This performance degradation is caused by intensified inter-rotor flow interference: the compact spacing accentuates cross-stream flow perturbations, while extreme tilting redirects downwash away from the axial direction, thereby weakening vertical thrust generation.

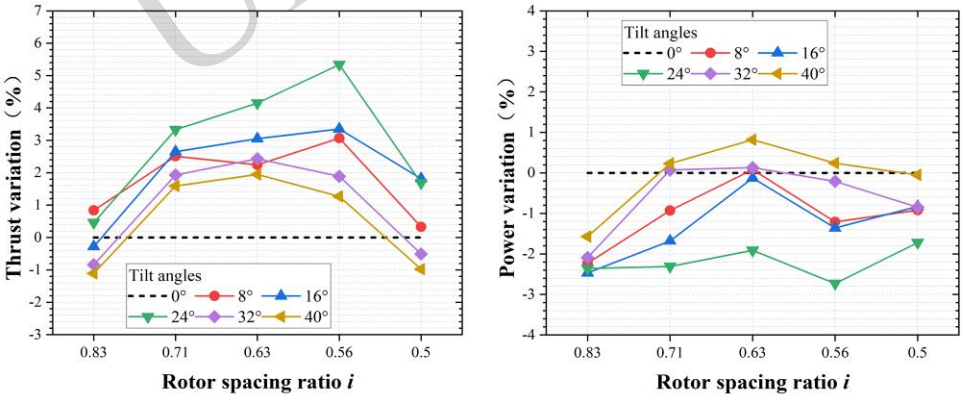

(a) (b)

Fig. 7 Thrust and power variation: (a) thrust variation. (b) power variation

In contrast, the configuration with i = 0.56 and θ = 24° achieves a 5.43% thrust increase relative to the planar design. This improvement arises because the 0.56 spacing ratio mitigates direct flow interference, enabling the moderate 24° tilt to promote convergent downwash and coherent vortex coupling. These effects enhance the axial velocity (which is consistent with Eq. (2)) without compromising vertical lift. Correspondingly, power consumption varies with the flow characteristics: compared to the planar configuration, the i = 0.56, θ = 24° configuration reduces the power by 2.73%, while the i = 0.63, θ = 24° configuration increases it by 0.82%. This power increase reflects amplified turbulent dissipation caused by unregulated interactions between rotors at extreme tilt angles, demonstrating how geometric

parameters govern the balance between constructive and destructive flow interference.

To quantify hovering efficiency and identify optimal configurations, Fig. 8 presents the variations in the figure of merit (FM), a metric that integrates thrust generation and power consumption. The results indicate that FM values are consistently higher for the rotor spacing ratio i = 0.56, reaching a peak of 0.637 at θ = 24°. This confirms that the externally tilted configuration achieves maximum hovering efficiency under these specific conditions, and warrants a detailed numerical investigation of the underlying flow field dynamics for this optimal case. Furthermore, in this figure we can see the contrasts between the FM trends of the tilted and conventional planar configurations, showing that the tilted design generally outperforms the planar design. The largest FM improvement of 11.15% occurs at i = 0.56 and θ = 24°, which is attributed to constructive flow interactions: the selected spacing minimizes disruptive turbulence, while the 24° tilt angle promotes downwash convergence and coherent vortex coupling, thereby enhancing the overall energy conversion efficiency.

Conversely, at i = 0.5 and θ = 40°, the FM decreases by 1.14% relative to the planar configuration. This decrease is attributed to aerodynamic disorganization caused by excessive tilting: the extreme angles disrupt axial downwash, intensify inter-rotor turbulent mixing, and weaken vertical lift. These results underscore that tilt angles must be carefully balanced in order to promote, rather than impede, beneficial flow synergy.

Fig. 9 illustrates the variation of power loading (PL) with the spacing ratio and tilt angle. At i = 0.56 and θ = 24°, the PL = value is 4.821, which is 3.77% higher than that of the planar configuration, demonstrating the superior load-carrying capability of this configuration. Notably, at i = 0.56 and θ = 32°, the PL reaches 4.832, representing a 4.02% increase over the planar configuration and a marginal 0.24% increase compared to the θ = 24° case. Such a slight discrepancy may originate from a relatively favorable thrust-power balance that is specific to this regime. However, at θ = 32°, the expansion of the central recirculation zone disrupts the coherence of the axial downwash, reducing the effective thrust component; compared to the 24° configuration, the thrust decreases by 3.46% to 3.85%. Although power consumption concurrently decreases due to flow separation, leading to a slightly higher PL ratio, this trend does not correspond to the actual aerodynamic efficiency. The overall hovering performance remains superior at θ = 24°. This is because the PL which reflects the thrust-to-power ratio does not fully capture the aerodynamic efficiency under hovering conditions.

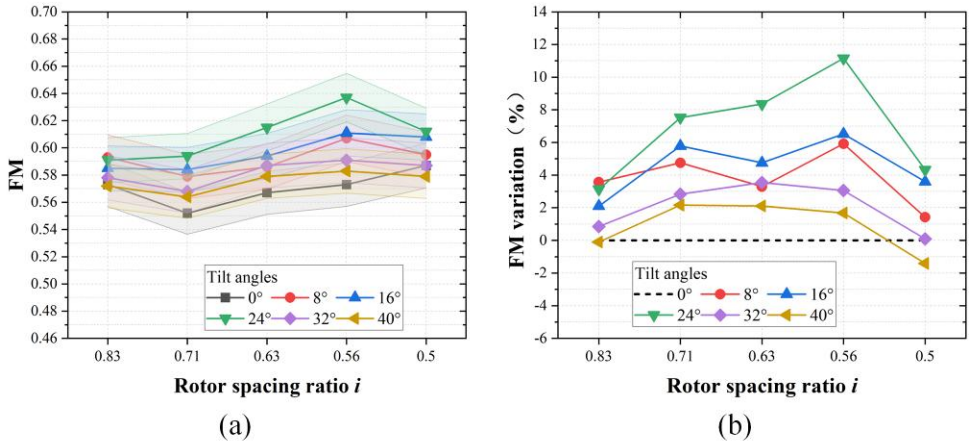

Fig. 8 FM variation (error bars represent 95% confidence intervals based on triplicate measurements)

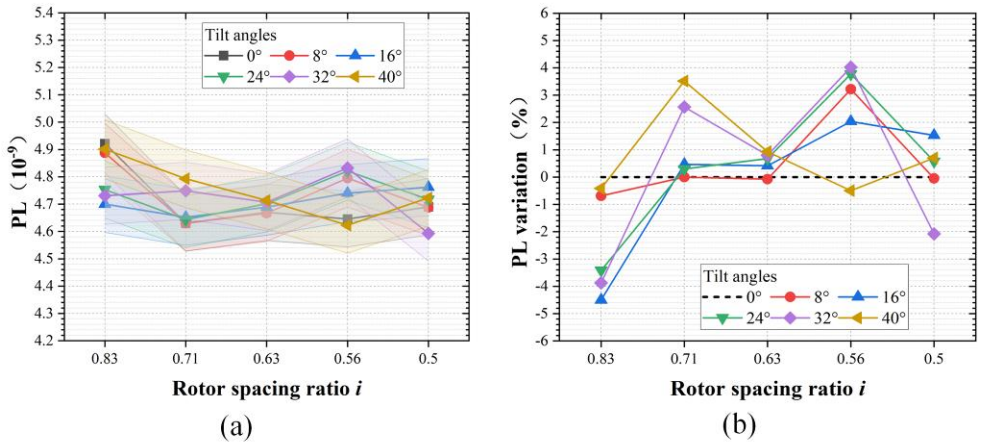

Fig. 9 PL variation (error bars represent 95% confidence intervals based on triplicate measurements)

Crucially, the FM, which is a unified efficiency metric integrating thrust and power coefficients, peaks at 0.637 for the 24° case, showing an 11.15% improvement. This confirms that FM, as opposed to PL alone, achieves synergistic optimization as it penalizes configurations where thrust loss is dominant. Consequently, the 24° configuration represents the aerodynamic optimum in this case, as it maximizes the FM, stabilizes the vortex dynamics, and preserves the downwash coherence metrics; these effects collectively outweigh the marginal PL advantage observed at 32°.

4.2 Simulation results

To characterize how tilt angles and inter-rotor interactions work together to govern the flow field, an analysis of downwash velocity distributions and streamline topology is essential. In particular, we want to uncover the specific mechanisms of aerodynamic optimization and rotor interference. The experimental results showed that FM exhibits a pronounced increase and notable variation near a rotor spacing ratio of i = 0.56. Therefore, focused numerical simulations of downwash velocity and streamline topology were performed for configurations adjacent to this spacing ratio, so as to investigate the fundamental flow mechanisms.

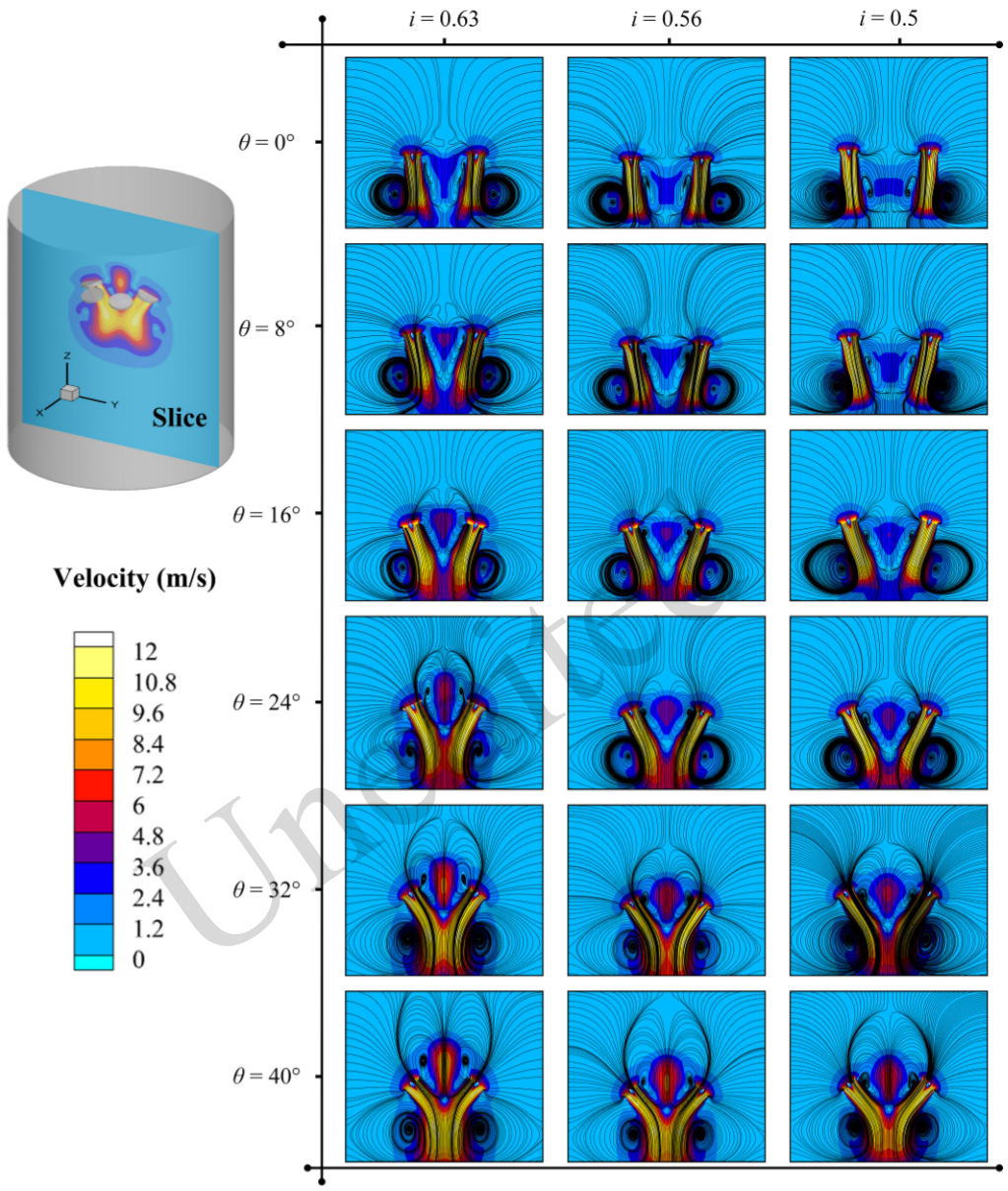

Fig. 10 Velocity contours and streamlines at different angles on the *zoy* plane for *i* = 0.63, 0.56, and 0.5

The flow field characteristics of the externally tilted hex-rotor configuration are presented in Fig. 10, providing detailed visualizations of velocity contours and streamlines for different angles at spacing ratios of $i = 0.63$, 0.56, and 0.5. At $\theta = 24°$, the configuration gains a significant aerodynamic advantage because of a favorable balance between thrust efficiency and inter-rotor flow interference, especially when $i = 0.56$. Unlike the planar configuration ($\theta = 0°$), the 24° tilt promotes coordinated airflow interactions between the rotors, which strengthens vortex coupling. Moreover, flow field analysis indicates that although the primary vortex cores beneath the rotors undergo mild perturbation, the dominant axial orientation of effective downwash is maintained. This balance enables the downwash streams to converge, thereby enhancing thrust by amplifying the axial velocity, an effect stemming from constructive flow superposition. The resulting moderately perturbed flow attains a functional balance: it meets the attitude control requirements inherent to tilted rotors without inducing the excessive flow destabilization observed at larger tilt angles. Simultaneously, the recirculation zones (shown in blue/purple) remain spatially

confined, with no substantial flow reversal or energy-dissipating turbulence, indicating optimized aerodynamic efficiency where thrust losses due to interference are minimized.

In contrast, at tilt angles beyond this optimal range (32° and 40°), the central recirculation zones expand noticeably and are accompanied by increased velocity fluctuations. This expansion disrupts axial downwash, reducing the effective flow velocity and compromising both thrust output and hovering efficiency. Over-tilting destabilizes the overall flow structure, leading to a 3.46% to 3.85% reduction in total thrust relative to the 24° configuration at $i = 0.56$. These results clearly indicate that extreme tilt angles shift the aerodynamic balance toward destructive flow interference.

Our analysis of the Fig. 13, which is supported by the experimental results, confirms that the configuration exhibits excellent aerodynamic performance at $i = 0.56$. Therefore, in subsequent simulation analyses we focus on this spacing ratio to examine aerodynamic characteristics at different tilt angles.

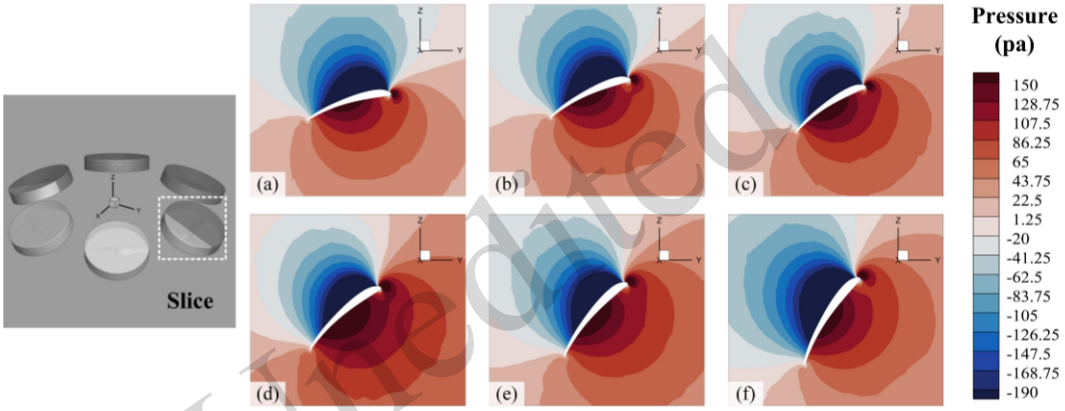

Fig. 11 Pressure distribution at the cross-section located at 3/4*R* for $i = 0.56$: (a) $\theta = 0°$; (b) $\theta = 8°$; (c) $\theta = 16°$; (d) $\theta = 24°$; (e) $\theta = 32°$; (f) $\theta = 40°$

Fig. 11 depicts the pressure distribution around the rotor units at various tilt angles, where red and blue regions correspond to high- and low-pressure zones, respectively. The pressure differentials, which govern aerodynamic force generation according to Bernoulli's principle, make the effective spatial organization of these zones critical for rotor efficiency.

At $\theta = 24°$, the pressure field shows smooth, organized streamwise gradients between high- and low-pressure regions. This well-ordered distribution signifies robust boundary layer attachment over the rotor surfaces and the absence of significant flow separations or stalling. These are characteristics of controlled airflow that enable high aerodynamic efficiency. The stable pressure differential facilitates consistent momentum transfer to the surrounding fluid, resulting in a 4.37% thrust increase compared to the planar configuration; this is consistent with the experimental measurements.

In contrast, at larger tilt angles (32° and 40°), the area of the high-pressure zone noticeably contracts. This contraction stems from flow detachment induced by excessive inclination: the excessive tilt disrupts the integrity of the boundary layer, intensifies turbulent mixing, and weakens the effective pressure differential. The consequential impairment of momentum transfer directly reduces hovering efficiency, illustrating how geometric tilt critically influences pressure-driven flow attachment.

Figs. 12 and 13 depict the vorticity fields on the *z*-normal plane and across the rotor system, respectively, and illustrate how tilt angles modulate rotational flow structures and inter-rotor aerodynamic interactions. At the optimal configuration ($i = 0.56$, $\theta = 24°$), both plots show concentrated and well-defined primary vortex cores with minimal diffusion, along with stable and symmetric vorticity patterns. This organized vortex structure signifies constructive vortex coupling, which acts to enhance downwash convergence and increase the effective axial velocity—these are

findings that align with the 5.43 % thrust increase and 11.15 % FM improvement observed in Figs. 7 and 8. At θ = 24°, the combination of constrained recirculation zones and preserved vortex integrity minimize turbulent energy dissipation while also maintaining uniform pressure gradients (Fig. 11d) and consistent rotor tip velocities (Fig. S4).

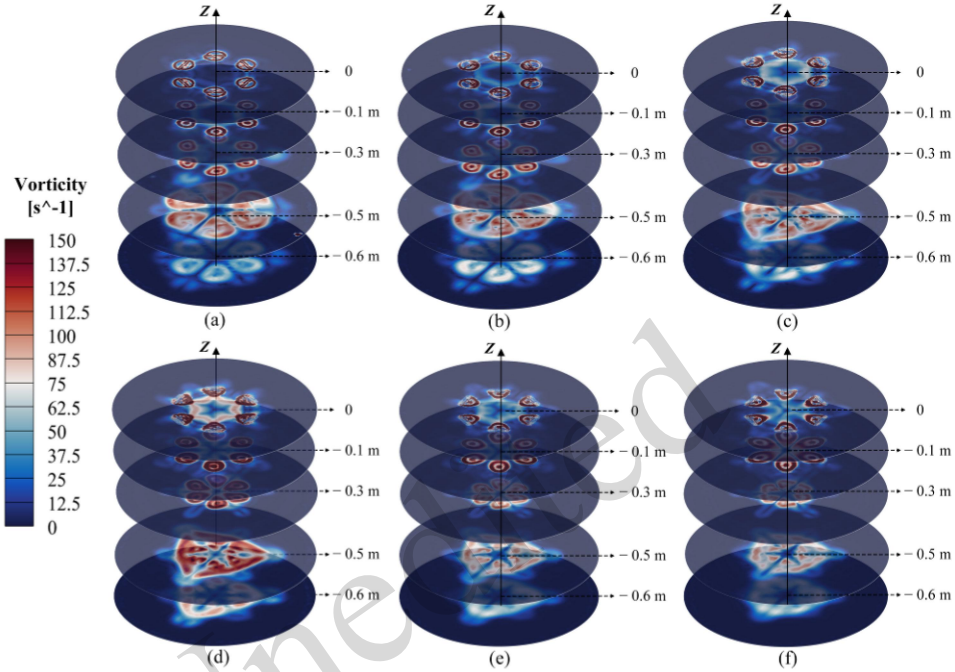

Fig. 12 Vorticity field visualization on the *z*-normal plane at *i* = 0.56: (a) θ = 0°; (b) θ = 8°; (c) θ = 16°; (d) θ = 24°; (e) θ = 32°; (f) θ = 40°

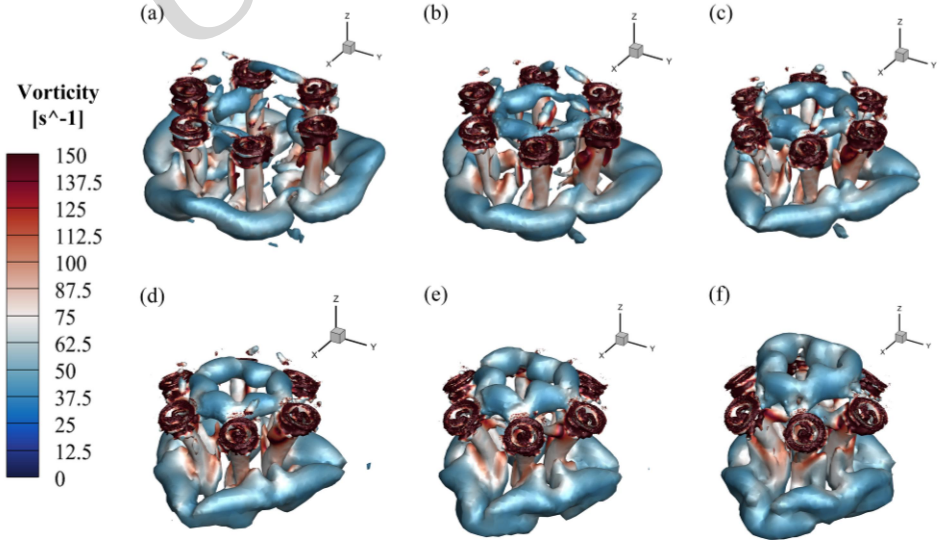

Fig. 13 Vorticity structure at *i* = 0.56: (a) θ = 0°; (b) θ = 8°; (c) θ = 16°; (d) θ = 24°; (e) θ = 32°; (f) θ = 40°

Conversely, larger tilt angles (32 ° and 40 °) induce diffuse and chaotic vorticity fields characterized by intensified flow separation and vortex breakdown. These flow disruptions enlarge regions of high vorticity, impair pressure differentials, and decrease thrust generation by 3.46% to 3.85%. Meanwhile, the planar configuration (θ = 0°) exhibits weak, symmetric vortices accompanied by limited downwash coherence, which accounts for its inferior performance.

These analyses confirm that moderate tilting combined with optimal spacing stabilizes vortex dynamics and accordingly leverages beneficial flow coupling, whereas excessive tilting disrupts vortex organization. This outcome highlights the critical role of vorticity structure in optimizing the aerodynamic performance of the externally tilted hex-rotor UAV.

In addition, we conducted simulations to analyze the velocity and pressure distributions on the rotor surface, which further validated the aerodynamic performance of the optimal configuration. For more details, please refer to Section S6 of the ESM.

Collectively, these findings confirm that the configuration with $i = 0.56$ and $\theta = 24°$ optimizes rotor performance by achieving coordinated velocity uniformity, stable pressure gradients, and controlled flow attachment; these are therefore key indicators of flow synergy in externally tilted hex-rotors.

5 Conclusions

In this study we systematically investigated the aerodynamic performance and flow field synergy of an externally tilted hex-rotor UAV in hovering.

1. An enhanced hovering efficiency stems from flow synergy under moderate tilting. At $\theta = 24°$, downwash effects converge, amplifying the axial velocity and thrust. The tilt also strengthens the inter-rotor vortex coupling, stabilizing primary structures and reducing turbulent loss. This organized flow suppresses cross-stream disturbances and confines recirculation, driving net efficiency gains.

2. A synergistic interplay was revealed between the spacing ratio i and tilt angle θ. Optimal spacing ($i = 0.56$) minimizes detrimental flow overlap while enabling constructive downwash coupling, stabilizing pressure gradients. When combined with $\theta = 24°$, this configuration promotes coherent vortices without flow separation. Larger angles disrupt this balance, causing boundary layer detachment and performance loss, and thus highlighting the need for coordinated geometric control.

3. The optimal configuration was identified as a spacing ratio of $i = 0.56$ and a tilt angle of $\theta = 24°$. Compared to the conventional planar baseline configuration, this arrangement yielded a 5.43% increase in thrust, a 2.73% reduction in power consumption, an 11.15% improvement in FM, and a 3.77% enhancement in PL. CFD simulations confirmed that this optimum corresponds to stabilized vortex dynamics, constrained recirculation, and coherent downwash, which are all manifestations of synergistic tilt- and spacing-controlled flow.

The present study was confined to static hovering conditions with a specific rotor diameter ($D = 240$ mm) and rotational speed ($\Omega = 5{,}500$ r/min), which potentially limits the direct applicability of the identified optimal configuration to other multirotor designs. Future work should extend this framework to a broader parametric space in order to establish scaling laws relating optimal geometry to rotor size and speed; this would help enhance generalizability. Furthermore, validation under dynamic flight conditions is essential to assess the robustness of the observed flow synergy during maneuvers and under disturbances. The introduced PL metric also suggests a promising direction for fixed-thrust optimization, in particular minimizing the power consumption for a given amount of lift. Lastly, by employing continuous optimization algorithms, instead of a discrete parameter sweep, more efficient exploration of the design space could be achieved, and potentially reveal non-intuitive optimal configurations.

Acknowledgments

This research was funded by the National Natural Science Foundation of China (No. 52275095), and Fujian Provincial Industrial Robot Basic Components Technology Research and Development Center (No. 2014H2004).

Author contributions

Hengxing YANG: investigation, methodology, validation, data curation, formal analysis, visualization, writing–original draft. Yao LEI: conceptualization, funding acquisition, validation, supervision, writing–review & editing. Jifu HU: Software, validation. Guobin SHI: data curation, validation.

Conflict of interest

Hengxing YANG, Yao LEI, Jifu HU, and Guobin SHI declare that they have no conflict of interest.

References

Bohorquez F, Rankins F, Baeder J, et al., 2003. Hover Performance of Rotor Blades at Low Reynolds Numbers for Rotary Wing Micro Air Vehicles. An Experimental and CFD Study. 21st AIAA Applied Aerodynamics Conference, p.2003-3930. https://doi.org/10.2514/6.2003-3930

Cerny M, Breitsamter C, 2020. Investigation of small-scale propellers under non-axial inflow conditions. *Aerosp. Sci. Technol.*, 106(4):106048. https://doi.org/10.1016/j.ast.2020.106048

Chen K, Shi Z, Tong S, et al., 2019. Aerodynamic interference test of quad tilt rotor aircraft in wind tunnel. *Proc. Inst. Mech. Eng., Part G: J. Aerosp. Eng.*, 233(12):4499-4511. https://doi.org/10.1177/0954410019852827

Deters R, Kleinke S, Selig MS, 2017. Static testing of propulsion elements for small multirotor unmanned aerial vehicles. 35th AIAA Applied Aerodynamics Conference, p.2017-3743. https://doi.org/10.2514/6.2017-3743

Farajollahi A, Rostami M, 2021. Aerodynamic performance of mutual interaction tandem propellers with ducted UAV. *Aerosp. Sci. Technol.*, 108:106399. https://doi.org/10.1016/j.ast.2020.106399

Frachetti MD, Berner J, Liu X, et al., 2024. Large-scale medieval urbanism traced by UAV-lidar in highland Central Asia. *Nature*, 634(8036):1118-1124. https://doi.org/10.1038/s41586-024-08086-5

Garofano-Soldado A, Heredia G, Ollero A, 2023. Aerodynamic interactions of non-planar rotor pairs and model derivation in ground approach. *Aerosp. Sci. Technol.*, 142(3):108672. https://doi.org/10.1016/j.ast.2023.108672

Garofano-Soldado A, Sanchez-Cuevas PJ, Heredia G, et al., 2022. Numerical-experimental evaluation and modelling of aerodynamic ground effect for small-scale tilted propellers at low Reynolds numbers. *Aerosp. Sci. Technol.*, 126(2):107625. https://doi.org/10.1016/j.ast.2022.107625

Gerdroodbary MB, Shiryanpoor I, Salavatidezfouli S, et al., 2024. Optimizing aerodynamic stability in compressible flow around a vibrating cylinder with deep reinforcement learning. *Phys. Fluids*, 36(12):124143. https://doi.org/10.1063/5.0241809

Ibuki T, Yoshioka H, Sampei M, 2022. Robust pose tracking control for a fully-actuated hexarotor UAV based on Gaussian processes. *J. Control, Meas., Syst. Integr.*, 15(2):201-210. https://doi.org/10.1080/18824889.2022.2125242

Jaroslawski T, Forte M, Moschetta JM, et al., 2022. Characterisation of boundary layer transition over a low Reynolds number rotor. *Exp. Therm. Fluid Sci.*, 130(2):110485. https://doi.org/10.1016/j.expthermflusci.2021.110485

Jiang N, Wang K, Peng X, et al., 2023. Anti-UAV: A Large-Scale Benchmark for Vision-Based UAV Tracking. *IEEE Trans. Multimed.*, 25:486-500. https://doi.org/10.1109/TMM.2021.3128047

Leishman JG, Syal M, 2008. Figure of merit definition for coaxial rotors. *J. Am. Helicopter Soc.*, 53(3):290-300. https://doi.org/10.4050/JAHS.53.290

Lei Y, Ji Y, Wang C, 2018. Optimization of aerodynamic performance for co-axial rotors with different rotor spacings. *Int. J. Micro Air Veh.*, 10(4):373-382. https://doi.org/10.1177/1756829318804763

Lei Y, Wang J, Yang W, 2021. Aerodynamic Performance of a Coaxial Hex-Rotor MAV in Hover. *Aerospace*, 8(12):378. https://doi.org/10.3390/aerospace8120378

Li C, Xue C, Bai Y, 2019. Experimental investigation on aerodynamics of nonplanar rotor pairs in a multi-rotor UAV. 14th IEEE Conference on Industrial Electronics and Applications, p. 911-915. https://doi.org/10.1109/ICIEA.2019.8834124

Luan C, Lei Y, 2025. Aerodynamic study of dihedral angle configurations on a hexacopter during horizontal airflow disturbances. *Phys. Fluids*, 37(10): 105108. https://doi.org/10.1063/5.0294437

Luo, J., Zhu, L., Yan, G., 2015. Novel Quadrotor Forward-Flight Model Based on Wake Interference. *AIAA J.*, 53(12): 1-12. https://doi.org/10.2514/1.J053011

Luo Y, AI T, HE Y, et al., 2023. Numerical investigation on unsteady characteristics of ducted fans in ground effect. *Chin. J. Aeronaut.*, 36(9):79-95. https://doi.org/10.1016/j.cja.2023.04.004

Maisto G, Garofano A, Acanfora V, et al., 2025. Redesigning UAV Vertical Tail Structures with Lightweight Eco-Friendly Carbon-Reinforced Polymers: A Generative Design-Based Approach. *J. Compos. Sci.*, 9(10):517. https://doi.org/10.3390/jcs9100517

Marris E, 2013. Drones in science: Fly, and bring me data. *Nature*, 498:156-158. https://doi.org/10.1038/498156a

Menter F, Kuntz M, Langtry RB, 2003. Ten years of industrial experience with the SST turbulence model. *HEAT MASS TRANSFER*, 4(1):625-632.

Moses B, Marco M, Roberto N, et al., 2016. Aerodynamics of Rotor Blades for Quadrotors. *arXiv*, 1601.00733. https://doi.org/10.48550/arXiv.1601.00733

Mu Z, Qin Y, Yu C, et al., 2023. Adaptive cropping shallow attention network for defect detection of bridge girder steel using unmanned aerial vehicle images. *J. Zhejiang Univ. Sci. A*, 24(4):243-256. https://doi.org/10.1631/jzus.A2200175

Piccinini R, Tugnoli M, Zanotti A, 2020. Numerical Investigation of the Rotor-Rotor Aerodynamic Interaction for eVTOL Aircraft Configurations. *Energies*, 13(22):5995. https://doi.org/10.3390/en13225995

Prabhu A, Liu X, Spasojevic I, et al., 2024. UAVs for forestry: Metric-semantic mapping and diameter estimation with autonomous aerial robots. *Mech. Syst. Signal Process.*, 208(3):111050. https://doi.org/10.1016/j.ymssp.2023.111050

Prothin S, Fernandez Escudero C, Doué N, et al., 2019. Aerodynamics of MAV rotors in ground and corner effect. *Int. J. Micro Air Veh.*, 11:175682931986159. https://doi.org/10.1177/1756829319861596

Quintana VA, Flores EAP, Merchan E, 2018. Multi-Objective

Design Optimization of a Hexa-Rotor With Disturbance Rejection Capability Using an Evolutionary Algorithm. *IEEE Access*, 6:69064-69074. https://doi.org/10.1109/ACCESS.2018.2878314

Russell C, Conley S, 2020. The multirotor test bed-a new NASA test capability for advanced VTOL rotorcraft configurations. Proceedings of the Vertical Flight Society 76th Annual Forum, Virtual: The Vertical Flight Society, p.1–12. https://doi.org/10.4050/F-0076-2020-16370

Sheidani A, Salavatidezfouli S, Stabile G, et al., 2023. Assessment of icing effects on the wake shed behind a vertical axis wind turbine. *Phys. Fluids*, 35(9):095135. https://doi.org/10.1063/5.0163684

Sina N, Amiri P, Danesh M, 2021. Optimal Path Planning and Control of a Hexarotor with Mass Uncertainty in the Presence of Dynamic Obstacles and Wind Using Sliding Mode and Adaptive PSO Algorithm. 29th Iranian Conference on Electrical Engineering, p.695-701. https://doi.org/10.1109/ICEE52715.2021.9544503.

Su J, Zhu X, Li S, et al., 2023. AI meets UAVs: A survey on AI empowered UAV perception systems for precision agriculture. *Neurocomputing*, 518:242-270. https://doi.org/10.1016/j.neucom.2022.11.020

Wang Y, Su Z, Benslimane A, et al., 2024. Collaborative Honeypot Defense in UAV Networks: A Learning-Based Game Approach. *IEEE Trans. Inf. Forensics Secur.*, 19:1963-1978. https://doi.org/10.1109/TIFS.2023.3318942

Wang Z, Henricks Q, Zhuang M, et al., 2019. Impact of Rotor–Airframe Orientation on the Aerodynamic and Aeroacoustic Characteristics of Small Unmanned Aerial Systems. *Drones*, 3(3):56. https://doi.org/10.3390/drones3030056

Yao C, Krieglstein J, Janschek K, 2018. Modeling and Sliding Mode Control of a Fully-actuated Multirotor with Tilted Propellers. IFAC-PapersOnLine, 51(22):115-120. https://doi.org/10.1016/j.ifacol.2018.11.527

Yang C, Yang Z, 2017. Proceedings of the 2017 International Conference on Applied Mathematics, Modelling and Statistics Application, p.403-409. https://doi.org/10.2991/ammsa-17.2017.91

中文概要

题　目：具有外偏转构型的六旋翼飞行器悬停气动优化

作　者：杨恒星[1]，雷瑶[1,2]，胡继府[1]，时国宾[3]

机　构：[1]福州大学，机械工程及自动化学院，中国福州，350116；[2]福州大学，流体动力与电液智能控制福建省高校重点实验室，中国福州，350116；[3]中山大学，智能工程学院，中国深圳，518000

目　的：本文旨在通过实验测量与计算流体动力学（CFD）模拟相结合的方法，系统研究旋翼间距比（i = 0.5–0.83）与倾斜角（θ = 0°–40°）对具有外偏转构型的六旋翼无人机在悬停状态下气动性能的影响，特别是推力、功率消耗、品质因数（FM）与功率负载（PL）的变化规律，并深入揭示倾斜构型下旋翼间流动相互作用的协同机制。研究致力于优化旋翼配置，通过提升下洗流汇聚与涡流耦合效应，抑制不利的流动干扰，从而提高悬停效率与有效载荷能力，为非平面多旋翼系统的气动设计与流动控制提供理论与实验依据。

创新点：1. 揭示了外倾斜六旋翼相对于传统平面构型提升悬停效率的流体动力学机制；2. 阐明了旋翼间距比（i）与倾斜角（θ）在调控推力生成中的协同作用机制；3. 确定了外倾斜六旋翼在悬停状态下的气动最优构型参数组合。

方　法：本研究采用实验测量与 CFD 模拟相结合的集成方法。首先，通过参数化实验，在定制测试台上系统测量了不同旋翼间距比（和倾斜角下的推力、扭矩和功率，并计算了品质因数和功率负载等性能指标。同时，利用高保真瞬态 CFD 模拟对相同工况进行数值计算，并通过网格无关性分析和实验数据验证确保了模型的可靠性。该方法通过实验获取宏观性能数据，并借助 CFD 深入揭示了下洗流汇聚、涡结构演化等内部流场协同机制。

结　论：1.适度的外倾斜（θ = 24°）能通过流场协同有效提升悬停效率。该角度促进了旋翼下洗流的汇聚，增强了轴向流速与推力；同时强化了旋翼间的涡流耦合，稳定了主涡结构，从而抑制了湍流损失。2. 旋翼间距比与倾斜角存在关键协同效应。最优间距比（i = 0.56）在减少有害流动重叠的同时，为有益的流场耦合创造了条件；与θ = 24° 结合，可实现稳定的压力梯度和涡结构，而过大倾角会破坏此平衡。3. 确定了气动最优构型（i = 0.56, θ = 24°）。相比传统平面构型，该配置实现了推力提升 5.43%、功耗降低 2.73%、品质因数提高 11.15%、功率负载增强 3.77%的综合优化，其流场表现为稳定的涡动力学和受约束的回流区。

关键词：无人机；空气动力学性能；悬停效率；转子间干扰；计算流体动力学